New insights into the vertical structure of the September 2015 dust storm employing 8 ceilometers over Israel

Leenes Uzan[1,2], Smadar Egert[1], Pinhas Alpert[1]

[1] Department of Geosciences, Raymond and Beverly Sackler Faculty of Exact Sciences, Tel-Aviv University, Tel Aviv, 6997801, Israel.
[2] The Israeli Meteorological Service, Beit Dagan, Israel.

Correspondence to: Leenes Uzan (Leenesu@gmail.com)

Abstract

On 7 September 2015 an unprecedented and unexceptional extreme dust storm struck the Eastern Mediterranean (EM) basin. Here, we provide an overview of the previous studies and describe the dust plume evolution over a relatively small area, i.e., Israel. This study employs multiple tools including an array of eight ceilometers, spectral radiometers (AERONET), ground particulate matter concentrations, satellite images, global/diffuse/direct solar radiation measurements and radiosonde profiles. Main findings reveal that the dust plume penetrated Israel on the 7 September from the northeast in a downward motion to southwest. On 8 September, the lower level of the dust plume reached 200 m above ground level, generating aerosol optical depth of AOD>3, and extreme particulate matter concentration measured on ground level up to ~10,000 μm m^{-3}. A most interesting feature on 8 September was the very high variability in the surface solar radiation in the range of 200-600 W m^{-2} (22 sites) over just a distance of several hundred km in spite of the thick dust layer above. Furthermore, 8 September shows the lowest radiation levels for this event. On the following day, 9 September, the surface solar radiation increased, thus enabling a late (~ 11 UTC) sea breeze development mainly in the coastal zone along with 5 m s^{-1} surface winds associated with arc-shaped dust layers. On 10 September the AOD values started to drop to ~ 1.5, the surface concentrations of particulate matter decreased as well as the ceilometers aerosol indications; Still, as indicated by CALIPSO a 2-4 km dust layer remained.

1. Introduction

An exceptionally extreme dust storm prevailed over the Eastern Mediterranean (EM) on September 2015. The Israeli meteorological service (IMS) declared the dust storm to be extraordinary as it occurred on early September (7-10 September), extended over a time span of 100 hours creating extreme ground level particulate matter (PM) concentrations (e.g. 100 times above the hourly average of PM10 in Jerusalem). On 7 September, prior to the penetration of the dust storm over Israel, IMS reported (http://www.ims.gov.il/IMS/CLIMATE; in Hebrew) a heat wave which prevailed over Israel causing harsh weather conditions of 80-90% relative humidity, 42 ℃ in valleys, 38 ℃ in mountains. On 8 September, visibility decreased below 3 km and consequently, inland aviation was prohibited until the 9 September (Fig.1). Concurrently, severe ground level PM concentrations resulted a public warning from outdoor activities, issued by the environmental protection ministry. Finally, on 11 September, as visibility increased, the IMS confirmed the dust storm ended, whereas the heat wave was over only two days later, on 13 September, subsequent to a profound change in weather conditions. The PM concentrations declined to values measured prior to the dust storm (http://www.svivaaqm.net/Default.rtl.aspx; in Hebrew) only on 14 September, though the AERONET measurements (https://aeronet.gsfc.nasa.gov) stationed in central and southern Israel reveal that the aerosol optical depth (AOD) resumed to values prior to the dust storm only on 17 September.

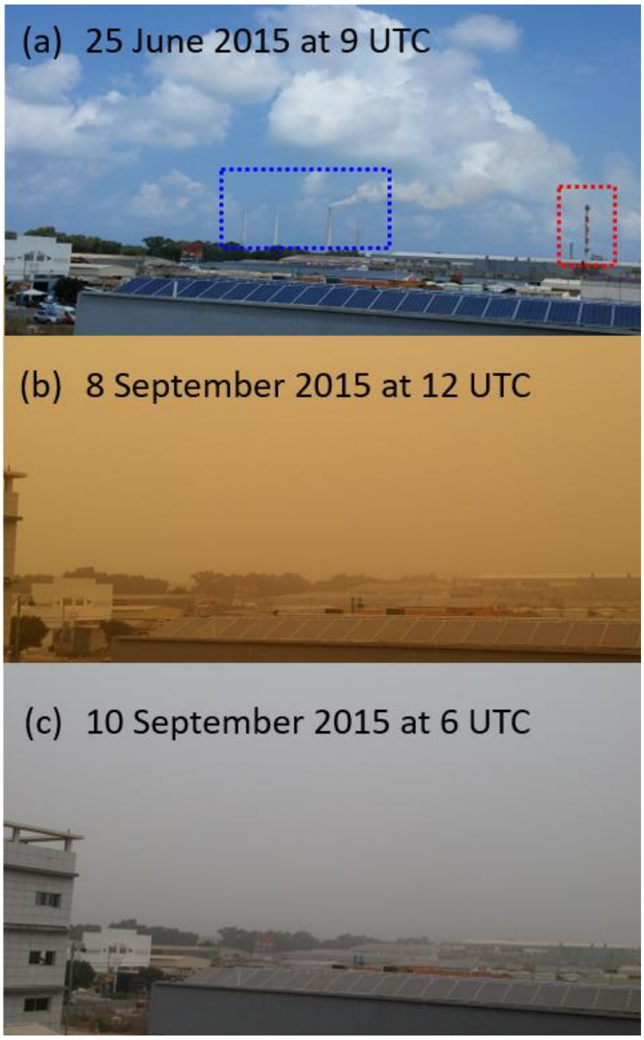

Figure 1. Photographs taken from the central coast of Israel, adjacent to the Hadera ceilometer, 3.5 km southeast to the stacks of a power plant (indicated by a blue rectangle) and 600 m north to a factory stack (indicated by a red rectangle). The photographs were taken prior to the dust storm, on 25 July 2015 (a) and during the dust storm, on 8 September 2015 (b) and 10 September 2015 (c). Notice that during the dust event (b,c) the stacks clearly seen in (a) from the same spot, are invisible.

Investigation of the mechanisms leading the severe dust storm was performed by Gasch et al. (2017) using a state of the art dust transport model ICOsahedral Nonhydrostatic (ICON) with the Aerosol and Reactive Trace gases (ART) (Rieger, et al., 2015). The model concentrated on the EM with one global domain (40 km grid spacing, and 90 vertical levels from 20 m to 75 km) and 4 nested grids (20, 10, 5 and 2.5 km grid spacing and 60 vertical levels from 20 m to 22.5 km). Simulations were done for three consecutive days from 6-8 September. Model results delineated an unusual early incidence of an active Red Sea Trough (Fig.2; Alpert et al, 2004) over Mesopotamia, followed by meso-scale convective systems over the Syrian-Iraqi border generating three cold-pool outflows. On the night between 5 and 6 September, a convective system fueled by an inflow along the eastern side of the Red Sea Trough, moved northeast over the Turkish-Syrian border region. The convective system intensified overnight and generated a first weak cold pool outflow on the 6 September. After sun rise, as the nocturnal boundary layer dissipated, an increase of downward mixing lead to an increase of surface wind speeds consequently causing dust to pick up over Syria. The high surface wind speeds sustained during the day due to a strong and shallow heat low whereas sea breeze transported dust to the south towards Jordan. At this point, the atmospheric instability over the Syrian-Iraqi border created a second convective cool outflow from the Zagros mountain range west into Syria. The gust from the second cool pool outflow ignited a third cool pool outflow at 20 UTC. The third outflow moved southerly along the eastern flank of the Red Sea Trough and shifted warm and moist air masses along the way. Past midnight, on 7 September, the intensified third cool pool outflow shifted to the west. At 10 UTC 7 September, rainfall and an increase of surface wind speeds north-west of Syria strengthened the third cool pool outflow. Consequently, enormous dust emissions transported southwest up to 5 km. The aged second cool pool outbreak re-intensified over Jordan and southwestern Syria and merged with the third outflow with the nightfall of 7 September. After midnight, on 8 September, the dust transported over Israel and was mostly influenced by local circulation systems in the EM. Model simulations were compared to in-situ measurements and satellite images: visible electromagnetic spectrum from Moderate Resolution Imaging Spectroradiometer (MODIS: https://modis.gsfc.nasa.gov/) aboard the Aqua satellite; AOD from the Terra satellite; RGB dust product from the Spinning Enhanced Visible and InfraRed Imager (SEVIRI) upon the Meteosat Second Generation (MSG) satellite; total attenuated backscatter from Cloud-Aerosol Lidar upon the Infrared Pathfinder Satellite Observations (CALIPSO: https://www-calipso.larc.nasa.gov/). Ground level meteorological measurements (3 sites) and PM concentration (3 sites) in Israel were employed. Results revealed the model lacked sufficient development of a super critical flow, which in effect produced the excessive surface wind speeds. Eventually, this misled the forecast of the dust advection southwest into Israel.

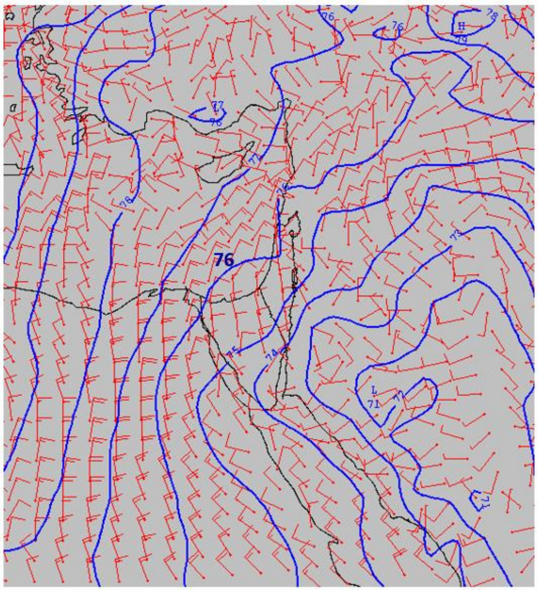

Figure 2. 925 mb map from 7 September 2015 12 UTC of the geopotential height with 1 dm interval (the 76 dm line passing over Israel; blue lines) and wind (10 KT each line; red arrows). Source: IMS from UKMO British Met Office model.

The fact that forecast models did not succeed in predicting this outstanding dust event motivated Mamouri et al. (2016) to study its origin and development. Their research presented dust load observations in the Cyprus region. Luckily, at the time of the dust storm, an EARLINET (European Aerosol Research lidar Network: https://www.earlinet.org/) Raman lidar stationed in Limassol provided vertical dust profiles and valuable optical dust properties of backscatter, extinction, lidar ratio and linear depolarization ratio. They analyzed the optical thickness (AOT) and Angström exponent derived from the MODIS Aqua satellite. MODIS Aqua AOT measurements were compared to the Limassol lidar observations, AOD measurements from two AERONET sites (Cyprus and Israel) and ground level PM10 concentration from four Cyprus sites. On 7 September, EARLINET lidar observations measured two dust layers (extending up to 1.7 km ASL and between 1.7-3.5 km ASL). The dust particle extinction coefficient measured in Limassol had reached 1000 Mm^{-1} followed by high PM10 concentration of 2000 $\mu m\ m^{-3}$. Extreme values over Limassol, were reported on the 8 September as MODIS Aqua AOT observations exceeded 5 (assuming overestimation up to 1.5) and hourly PM10 concentration of about 8,000 $\mu m\ m^{-3}$ (with uncertainties in the order of 50%). Unfortunately, on the 8 September, the lidar was intentionally shut down to avoid potential damage to the instrument. Nevertheless, lidar observations indicated another dense dust outbreak (1-3 km ASL) reaching Limassol on the 10 September, also visible by the MODIS Aqua AOT imagery. The researchers concluded the scale of the dust storm features was too small for global and regional dust transport models. They presumed that the initiation of the dust plume was due to an intense dust storm (Habbob) in northeastern Syria and northern Iraq, leading to vigorous downbursts which consequently pushed huge amounts of dust and sand to the atmosphere. The lidar observations indicated a double layer structure of the dust, 1.5 and 4 km above sea level (ASL), pointing to multiple dust sources.

Stavros et al., (2016) continued the investigation of the formation and mechanism of the dust storm over Cyprus by a high regional atmospheric model of the integrated community limited area modeling system (RAMS-ICLAMS). The model simulations focused on the generation of the dust storm on 6 and 7 September. Model results were fine-tuned by observations from EARLINET lidar stationed in Limassol, radiosonde data from five sites (Cyprus, Israel, Jordan, and two from Turkey) and satellite imagery from MSG SEVIRI and CALIPSO CALIOP. The model was set to three grid space domains: an external grid of 12X12 km, (over the EM) an inner set at 4X4 km (over northern EM) and 2X2 km grid for cloud resolving (over northeastern Syria). The vertical structure consisted of 50 terrain following levels up to 18 km. The researchers assessed a strong thermal low over Syria followed by convection activity over the Iraq-Iran-Syria-Turkey borderline combined with land use changes (aftermath of the war held in Syria) manufactured the extreme dust storm. The model succeeded to describe the dust westward flow of a haboob containing the dust previously elevated over Syria as observed by MSG SEVIRI and EARLINET lidar. However, there were some inaccuracies in the quantification of dust mass profiles. They attributed the model discrepancies to the limited ability of the model to properly resolve dust and atmospheric properties (e.g. change of land use and intense downward mixing).

Evaluation whether the dust activation due to human perturbations to land use (such as in the Syria civil war) had an underlying effect on the dust storm formation or even to its increase were studied by Pu and Ginoux, (2016). They examined the connection between the Pacific decadal oscillation and the dust optical depth (DOD) in Syria. DOD, derived by the deep blue algorithm (Hsu et al., 2013) aerosol product from MODIS Terra and MODIS Aqua satellite (10 km resolution picture) was combined with monthly horizontal winds and geopotential heights generated by the European Centre for Medium-Range Weather Forecasts (ECMWF) reanalysis (horizontal resolution of 80 km and 37 vertical levels). The dataset of DODs during the years 2003-2015 were compared to the Geophysical Fluid Dynamics Laboratory (GFDL) Atmospheric model (AM3) (Donner et al., 2011). The AM3 model produced AODs and calculated the mass distribution and optical properties of aerosols, their chemical production, transport, and dry or wet deposition. Comparison of AOD model results, AOD AERONET measurements and DOD from satellite observations revealed the model underestimated the AOD's particularly in the

EM. The authors assumed that the soil moisture parameter in the model were not set properly resulting in the AOD dissimilarities.

The impact of the conflict in Syria on the aridity of the region and therefore, a possible direct impact on the generation of the September dust storm was examined by Parolari et al., (2016). The researchers conducted simulations using the Advanced Research Weather Research and Forecasting (WRF-ARW) model from 30 August to 10 September over the EM. The model consisted of two nested domains (9 and 3 km grid spacing and 35 vertical levels). Daily and monthly AOD data from MODIS were computed by the deep blue algorithm over land. Anomalies of the September 2015 monthly average AOD were compared to the monthly average of 2000-2015. The monthly average of September 2015 vegetation status in the region was estimated by MODIS normalized difference vegetation index (NDVI). Historical data was divided into two periods: none-drought (2001-2006) and drought (2007-2010). Wind shear stress was calculated to estimate wind erosion. Their findings reveal that the enhanced dust uplift and transportation of the September 2015 dust storm was due to meteorological conditions rather than the land-use changes because of the civil conflict in Syria. WRF simulations revealed the well-known Shamal winds and cyclone associated with dust storms in the Middle East (Rao et al., 2003) were characterized by northwesterly winds west of the low pressure zone in the Syrian-Iraqi border. However, the source of elevated dust concentrations over the EM coast on the 7and 8 September were attributed cyclone front movement. On 6 September low level winds (700 hPa) were opposite to the northwesterly high level (300 hPa) winds, consequently, generating enhanced surface shear stress and transported re-suspended PM westward. Furthermore, based on the past 20 years, the Israeli summer of 2015 was unusually dry and hot and therefore enabled easier updraft of dust soil increasing the probability of dust emissions.

Jasmin (2016) compared the dust storm aerosol content provided by MSG SEVIRI observations, to the results of the open source Meteoinfo model (Wang, 2014). The Meteoinfo model was based on meteorological variables from ECMWF. The model meteorological conditions suggested a formation of two simultaneous dust storms, from northern Syria and from the Egyptian Sinai desert, resulting from updrafts created by low pressure systems.

The aforementioned studies (summarized in Table 1) focused on the generation of the dust storm in the Syria region based on transport models, satellite imagery and in situ measurements. In our study we focus on the evolution of the dust plume over Israel in the lower atmosphere based on an array of 8 ceilometers, 52 in situ PM measurements, two AERONET sites and satellite imagery. We do not investigate the reasons of the models frailer to predict this extraordinary storm, but rather attempt to present details of the evolution of the dust plume passage over Israel. The data presented here can be used as a tool to verify state of the art model simulations and provide a different point of view to the meteorological conditions governing the dust plume advection over the EM.

In the following section we describe the measuring sites and instruments in this study. The list of instruments includes; ceilometers, PM measurements, AERONET, radiosonde, solar radiation and satellite imagery. Sect. 3 presents the results of the dust plume spatial and temporal scheme delineated by the ceilometer plots on 7 September through the 10 September 2015. We discuss and compare between the ceilometer plots and the aforementioned auxiliary measurements. In Sect. 4 we conclude our main findings of the dust plume advection in the lower atmosphere above Israel and the downward transport towards the ground.

2. Instruments

2.1 Ceilometers

Ceilometers, initially intended for cloud level height detection, are automatic low cost lidars widespread in airports and weather stations worldwide. As single wavelength lidars, ceilometers cannot produce the information aerosol properties such as size distribution, scattering and absorption coefficients (Ansmann et al., 2011; Papayannis et al., 2008). Nevertheless, with improvement of hardware and firmware over the years, ceilometers have become a valuable tool in the study of the atmospheric boundary layer and the vertical distribution of aerosols layers (Haeffelin and Angelini, 2012; Ansmann et al., 2003). Furthermore, in 2013 ceilometers been assimilated in the EUMETNET (European Meteorological Services network) Profiling Program (E-profile) to develop a homogeneous dataset from automatic lidars and state-of-the-art ceilometers across Europe (http://eumetnet.eu/activities/observations-programme/current-activities/e-profile/alc-network/).

Vaisala ceilometers type CL31, are commonly deployed worldwide, and the main research tool in this study as well. CL31 is a pulsed elastic micro lidar, employing an Indium Gallium Arsenide (InGaAs) laser diode transmitter of near infrared wavelength of 910 nm ±10 nm at 25˚C. In order to compensate the low pulse energy of the laser (defined "eye-safe") and to provide sufficient signal to noise ratio, the pulse repetition rate is of 10 kHz every two seconds (Vaisala ceilometer CL31 user's guide: http://www.vaisala.com). The backscatter signals are collected by an avalanche photodiode (APD) receiver and designed into attenuated backscatter profiles within a reporting interval of 2-120 s (determined by the user). The attenuated backscatter profiles are automatically corrected by an internal calibration (resulting in a multiplication factor of 10^{-8} to convert the signal count to attenuated backscatter), a cosmetic shift of the backscatter signal (to better visualize the clouds base), an obstruction correction (when the ceilometers' window is blocked by a local obstacle) and an overlap correction (to the height where the receiver field of view reaches complete overlap with the emitted laser beam).

Kotthaus et al., (2016) examined the Vaisala CL31 ceilometer by comparing the attenuated backscatter profiles from 5 units with different specification of senor hardware, firmware and operation settings (noise, height and time reporting interval). They have concluded the instrument characteristics that affect the quality and availability of the attenuated backscatter profiles in the following manner: At high altitudes, a discontinuity in the attenuated backscatter profile is evident at two height points, ~ 4949 and 7000 m. Background signals (instrument related) and cosmetic shift (firmware dependent) tend to be either negative or positive up to 6000m and then switch signs above ~ 6000 m. Below 70 m an overlap correction is applied internally by the ceilometer sensor as well as an obstruction correction (below 50 m). Between 50-80 m hardware related perturbation cause a slight offset in the attenuated backscatter values. The authors advise the user-defined reporting interval should be no shorter than 30s to avoid consecutive profiles partial overlap. However, they emphasize the internal calibration applied to convert the signal count output to "attenuated backscatter" does not always fully represent the actual lidar constant, therefore, it is not accurate enough for meteorological research. Nevertheless, since ceilometers are not sensitive to molecular scattering and solar radiation contributes to the random noise, a background correction can be derived by a 4 hr round of midnight attenuated backscatter profiles. Furthermore, a range corrected attenuated backscatter can be derived by the attenuated backscatter profiles during an existence of a stratocumulus cloud.

Furthermore, Weigner et al, (2014) studied different retrieval methods to derive the aerosol backscatter coefficient from the ceilometers' attenuated backscatter profiles based on a comparison to auxiliary collocated instruments such as a sunphotmeter or a multiwavelength lidar. They focused on calibration methods, the rage detection limitations by the overlap function and the sensitivity of the attenuated backscatter signal to relative humidity. Although, the ceilometer wavelength range (given as 905 ±3 nm) is influenced by water vapour absorption, in the case of aerosol layer detection, water vapour distribution has a small effect on the signal change, indicating the mixed layer height (MLH) or an elevated mixed layer, as the aerosol backscatter itself remains unchanged. Consequently, except for a case of a dry layer in a humid MLH, the water vapour is unlikely to lead misinterpretation of the aerosol stratification. Fortunately, most algorithms are based on a significant signal slope to define the aerosol layers, therefore, can be determined from uncelebrated ceilometer attenuated backscatter profiles. The wavelet covariance transform (WCT) was the method used in this study to evaluated the MLH (Uzan, et al, 2016), whether determined by the creation of thermals or the subsidence of the dust plume.

In this study, we address the aforementioned limitations as we refer to the ceilometer signal count profiles between 100-1000 m AGL. The ceilometer array is comprised of 8 units in different sites (Fig 3 and Tables 2-3), 6 of which are owned by a governmental office. The ceilometers are CL31 type apart for ceilometer CL51 stationed in the Weizmann Institute which has a higher backscatter profile range (up to 15.4 km, Münkel et al., 2011). Unfortunately, calibration procedures were not held and maintenance (cleaning of the ceilometer window) was done regularly only for the Beit Dagan ceilometer. Apart from the Beit Dagan and Weizmann ceilometers (Table 4), we could not retrieve the technical information of firmware and hardware type. However, we have been confirmed (personal communication) that the combination of hardware and firmware had been done following Kotthaus et al (2016). The Beit Dagan ceilometer signal count were found to be weaker (up to 800 signal count compared to 10,000 in the other CL31 ceilometers) due to different hardware definitions. Therefore, in order to present the Beit Dagan attenuated backscatter profiles aligned with the profiles of the other ceilometers (given in Fig. 17), the Beit Dagan attenuated backscatter values were multiplied by 12.5 (10,000/800).

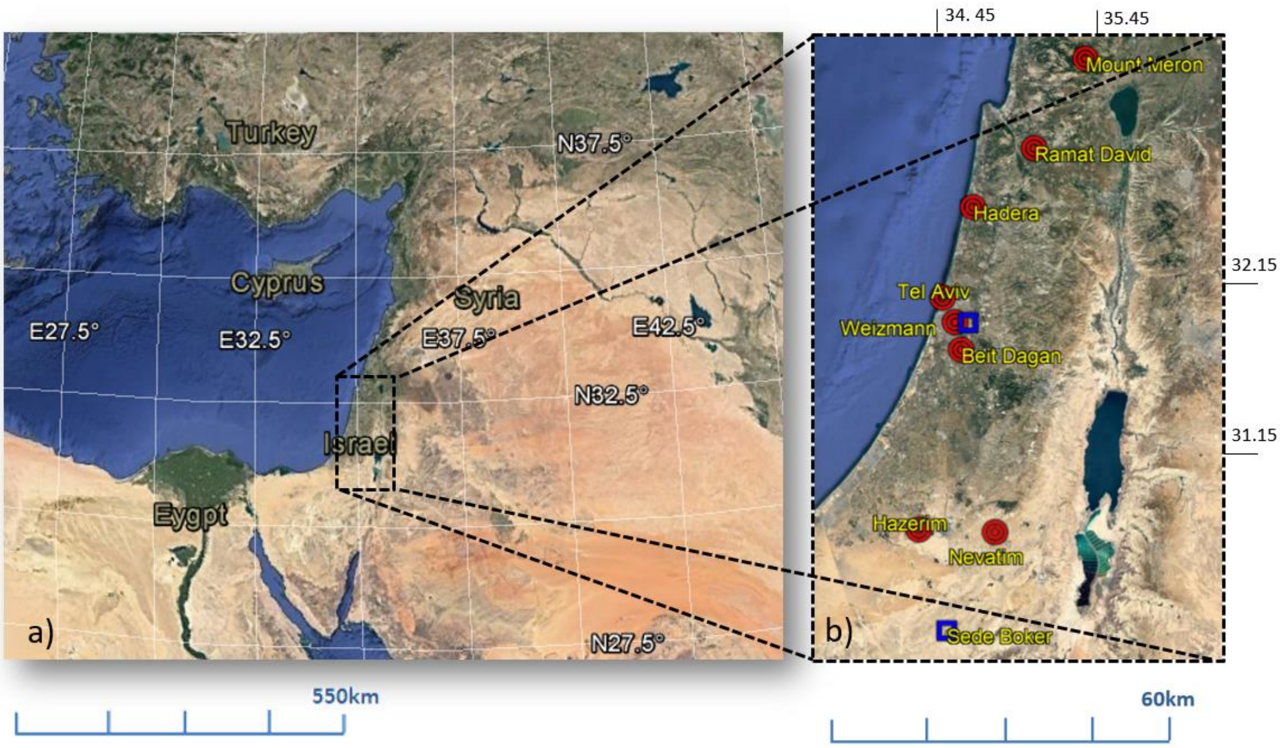

Figure 3. Google Earth map of the large domain (a) and Israel (b) with indications of 8 ceilometer sites (red circle; detail in Table 2) and two AERONET sites (blue square).

2.2 Radiosonde

Radiosonde (RS) type Vaisala RS41-SG is launched by the IMS twice a day at 00 UTC and 12 UTC from the Beit Dagan site adjacent to the Beit Dagan ceilometer. The radiosonde produces profiles of humidity, temperature, pressure, and wind speed and wind direction. The output files were downloaded from the University of Wyoming site (http://weather.uwyo.edu/upperair/sounding.html, station number 40172). With respect to Stull (1988), the MLH was defined by the RS profiles as the height where the following phenomena were identified: an inversion in the temperature, a significant drop in the relative humidity, strong wind shear and an increase in the virtual temperature (Uzan et al., 2016; Levi et al., 2011).

2.3 Particulate matter monitors (PM10, PM2.5)

PM monitors are low-volume flow rate Thermo Fisher Scientific type FH 62 C14 (beta attenuation method) and type 1405 TEOM (Tapered Element Oscillating Microbalance method). In the beta attenuation method (https://www3.epa.gov/ttnamti1/files/ambient/inorganic/overvw1.pdf) low-energy beta rays are focused on deposits on a filter tape and attenuated according to the approximate exponential function of particulate mass (i.e., Beer's Law). These automated samples employ a continuous filter tape. The attenuation through an unexposed portion of the filter tape is measured, the tape is then exposed to the ambient sample flow where a deposit is accumulated. The beta attenuation is repeated, and the difference in attenuation between the blank filter and the deposit is a measure of the accumulated concentration. The weighing principle used in the TEOM method (https://tools.thermofisher.com/content/sfs/manuals/EPM-TEOM1405-Manual.pdf) is based on a mass change detected by the sensor as a result of the measurement of a change in frequency. The tapered element at the heart of the mass detection system is a hollow tube, clamped on one end and free to oscillate at the other. If additional mass is added, the frequency of the oscillation decreases. An electronic control circuit senses oscillation adds sufficient energy to the system to overcome losses. An automatic gain control circuit maintains the oscillation at a constant amplitude. A precision electronic counter measures the oscillation frequency with a 10-second sampling period. Both instruments report PM concentration every 5 min. The location of PM measurement sites is given in Tables 5.

2.4 AERONET

AErosol RObotic NETwork (AERONET) is multiband photometer with an automatic sun tracking radiometer for direct sun measurements with a spectral range of 340 to 1640 nm wavelengths. The photometer measures the solar extinction in each wavelength to compute aerosol optical depth (Holben et al., 1998). In Israel two AERONET units type CE318-N (https://aeronet.gsfc.nasa.gov) operate in Sede Boker and the Weizmann Institute (Fig. 3). Unfortunately, the unit in Weizmann did not operate during 6-8 September 2015 due to power failure. In this study we used AERONET Level 2.0 data (cloud screened and quality assured for instrument calibration) for AOD at 500 nm and the Ångstrom Exponent defined by 440-870 nm.

2.5 Global, direct and diffuse solar radiation measurements

Global radiation measured in by IMS in 22 sites (Table. 6) by instrument type Kipp & Zonen pyranometer CMP-11. Integrated solar radiation (W m-2) from 300 to 3000 nm is produced every 10 min. Diffuse and direct radiation also measured in Beit Dagan (coastal region, 31 m ASL) and Beer Sheva (southern region, 71 m ASL). For diffuse radiation, a ring is installed over the pyranometer to shade direct solar radiation. Direct radiation is measured by a sun tracker pyrheliometer.

2.6 Satellite imagery

2.6.1 SEVIRI (MSG satellite)

Meteosat Second Generation (MSG) is a new series of European geostationary satellites operated by EUMETSAT (European Organization for the Exploitation of Meteorological Satellites). On board the MSG is a 12-channel Spinning Enhanced Visible and Infrared Imager (SEVIRI) (Roebeling et al., 2006). The combination of red, blue and green (RGB) channels (12-10.8 µm, green:10.8-8.7 µm, blue:10.8 µm, respectively) produce imagery of dust in pink or magneta, dry land in pale blue at daytime and pale green at nighttime, thick high-level clouds in red-brown tones and thin high-level clouds nearly black (http://oiswww.eumetsat.int/). Access to EUMETSAT imagery is given in https://www.eumetsat.int/website/home/Images/RealTimeImages/index.html. Several studies (Romano et al., 2013; Bennouna et al., 2009; Jolivet et al., 2008) compared AOD from MGS SEVIRI and AERONET measurements clarified the uncertainty of MSG SEVIRI AOD decreases as AOD rises. For continental aerosol type, errors do not exceed 10 % in viewing zenith angles between 20° and 50°, probable for the study area considered here. Overall, the MSG SEVIRI AOD uncertainty it is expected to be under 15% (Mei et al, 2012). North Africa Sand storm survey (NASCube: http://nascube.univ-lille1.fr) obtains AOD by temperature anomalies of SEVIRI RGB by the difference in emissivity of dust and desert surfaces during daytime.

2.6.2 MODIS (Terra and Aqua satellites)

The MODerate resolution Imaging Spectrometer (MODIS) instrument flies aboard the Earth Observation System's (EOS) Terra and Aqua polar-orbiting satellites, with Terra on a descending orbit (southward) over the equator about 10:30 local sun time, and Aqua on an ascending orbit (northward) over the equator about 13:30 local sun time. MODIS performs measurements by 36 channels between 412 to 14200 nm whereas the aerosol retrieval makes use of seven channels (646, 855, 466, 553, 1243, 1632 and 2119 nm central wavelength), and a number of other wavelength bands associated with screening procedures. As land signals (AERONET) and the atmospheric signals are comparable at ~ 550 nm, errors of 0.01 in assumed surface reflectance will lead to errors on the order of 0.1 in AOD retrieval (Remer et al., 2006).

2.6.3 CALIOP (CALIPSO satellite)

The Cloud-Aerosol Lidar with Orthogonal Polarization (CALIOP) is a two-wavelength polarization lidar (1064 and 532nm) that performs global profiling of aerosols and clouds in the troposphere and lower stratosphere. CALIOP is the primary instrument on the Cloud-Aerosol Lidar and Infrared Pathfinder Satellite Observations (CALIPSO) satellite. CALIOP is required to accurately measure signal returns from the aerosol-free region between 30 and 35 km as well as the strongest cloud returns. Samples acquired below 40 km for the 532-nm channel and below 30 km for the 1064-nm channel are downlinked as profile data. Data used here was based on level 2 version 4-10 CALIPSO product, spatial resolution of 5 km (20N-50N, 20E-50E) and vertical resolution of 60 m (limited up to 6 km).

3. Results and discussion

The following description of the dust event will proceed chronologically from 7 to 10 September and include main findings of the instruments (Sect. 2). The order of the instruments described follow the most interesting features revealed, not necessarily in the same order for each day.

On 7 September, images from MODIS Aqua (Fig. 4a) and MODIS Terra (Fig. 4e) taken between 07:20-12:10 UTC show that the dust plume progressed from northeast in a near-circular motion over the Mediterranean Sea. The penetration of the dust plume to Israel was indicated at ~ 05 UTC by an increase in AOD along a decrease in the Angström exponent (Fig. 5) from AERONET Sede Boker site. The relationship between the Angström exponent decrease and the mineral dust was pointed out by Mamouri et al., (2016). They studied the dust layer particle linear depolarization by an EARLINET lidar stationed in Limassol Cyprus and concluded that the linear depolarization ratio of 0.25-0.32 on 7,10 September, indicated the dominance of the mineral dust. In addition, an increase in the PM concentration started at ~ 05 UTC (not shown) reaching the highest hourly values of 107 µg m^{-3} PM2.5 (Table 5) and 491 µg m^{-3} PM10 (Table 6) only in the Jerusalem elevated sites and only at 22 UTC. This 17-hour gap is shown by the ceilometers' plots (Fig. 6-12) of a downward motion of the dust plume from ~ 04 UTC in all measuring sites except for the elevated Mount Meron site (1150 m ASL, Fig. 13). Following Gasch et al (2017) cold pool outflows concept, the exception of Mount Meron site is supported by the MSG-SEVIRI picture (Fig. 14) showing that the first dust plume was fragmented (Fig.14, red arrow) and the second dust plume (Fig.14, black arrow) had not passed over Israel before 12 UTC.

The full picture of what happened on the 7 September can be further obtained from the MSG-SEVIRI picture at 12 UTC that shows AOD to be still under 1 in most parts of Israel (Fig. 15). At the same time, Beit Dagan radiosonde profiles show the MLH was still high (700 m ASL, Fig. 16). And, ceilometers' profiles at 23 UTC (Fig. 17 a) show indications of typical cloud presence from 400 m ASL in the shoreline site (Tel Aviv, 5 m ASL) and up to ~700 m ASL in the elevated southern site (Nevatim, 400 m ASL). Clouds are identified by the peak shape of the profiles (Uzan et al, 2016) and the high attenuated backscatter of 10^{-1} m^{-1} sr^{-1} which in this case is 4 orders of magnitude higher than the attenuated backscatter of the dust plume (shown in Fig 17 b-c). In spite of the still high MLH and the cloud presence, the solar radiation measurements clearly indicates the significance of the dust plume effect through the decrease of the daily direct radiation along with an increase of the diffuse radiation (Fig. 18, see 7 September daily variation) measured both in central Israel (Beit Dagan) and southern Israel (Beer Sheva).

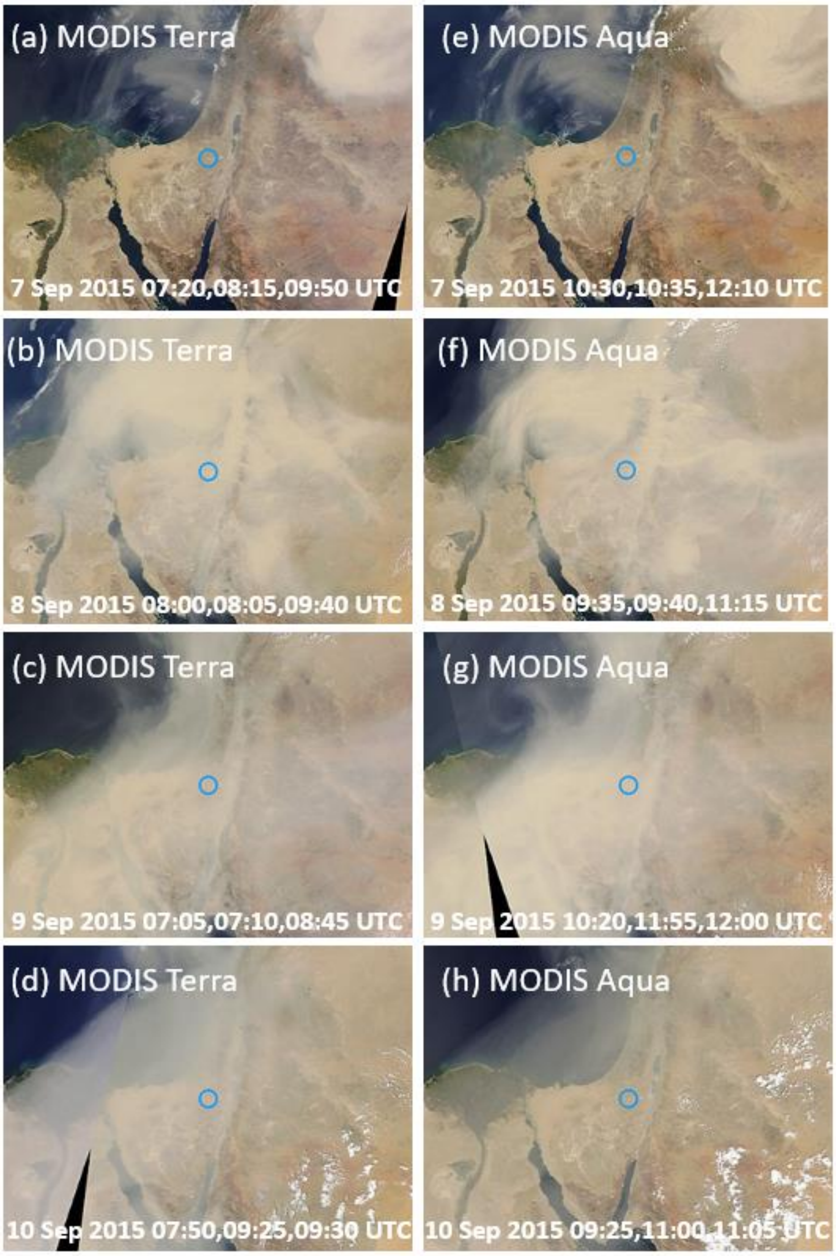

Figure 4. Pictures from MODIS terra (a-d) and MODIS Aqua (e-h). The date and time of overpass are indicated on each figure. Blue circle indicating the AERONET Sede Boker site. Source: https://aeronet.gsfc.nasa.gov.

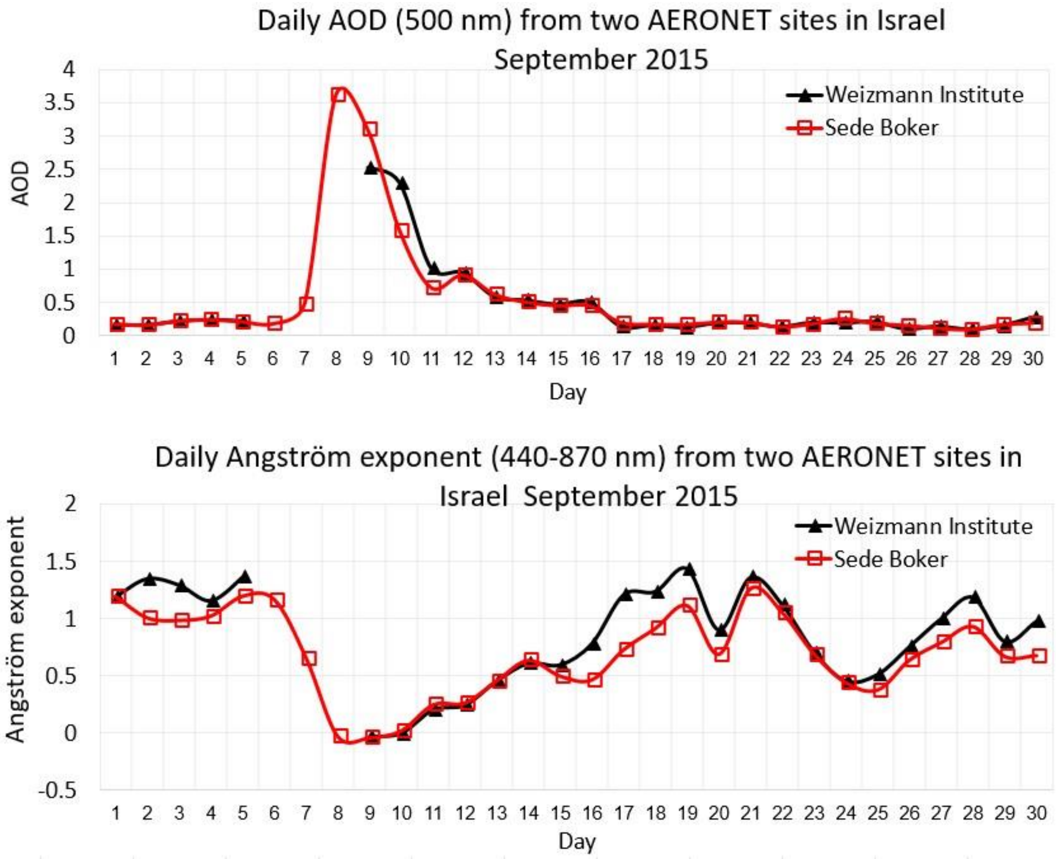

Figure 5. September 2015 daily average of AOD (top panel) and Angström exponent (bottom panel) from two AERONET sites in Israel (Sede Boker and Weizmann, see Fig.3). The Weizmann AERONET did not operate on 6-8 September due to power failure.

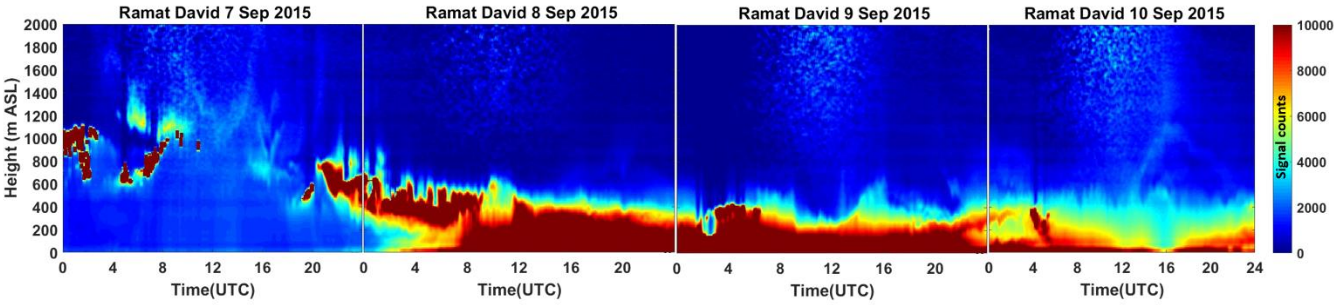

Figure 6. Ramat David ceilometer signal counts plots for 7-9 September 2015. Y-axis is the height up to 2000 m ASL, X-axis is the time in UTC, signal count scale range between 0-10,000.

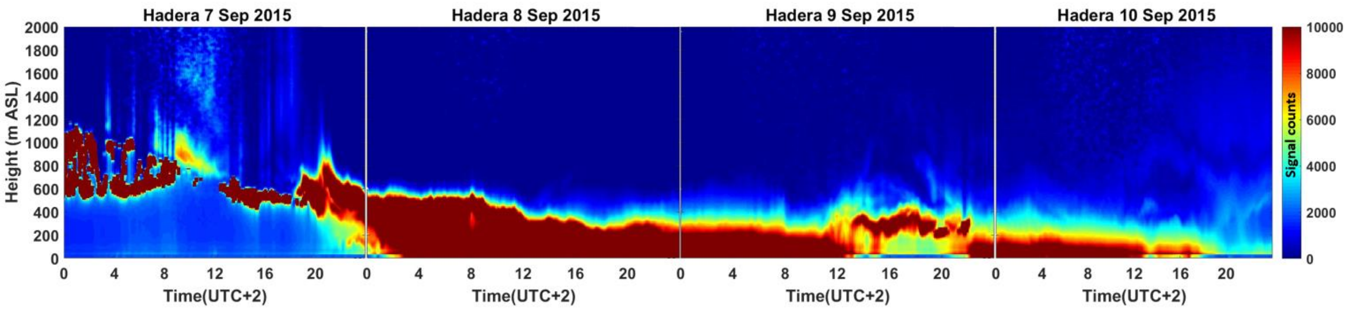

Figure 7. Hadera ceilometer signal counts plots for 7-9 September 2015. Y-axis is the height from site deployment to 2000 m ASL, X-axis is the time in LST (UTC+2), signal count scale range between 0-10,000.

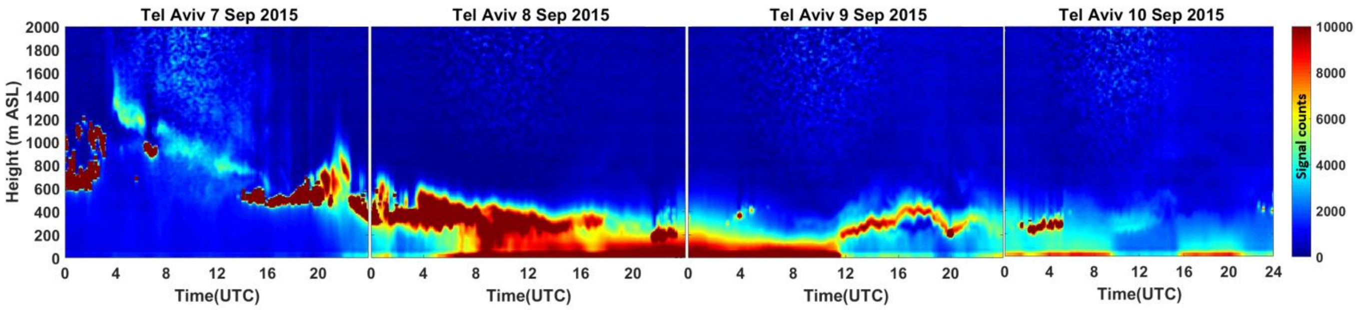

Figure 8. Tel Aviv ceilometer signal counts plots for 7-9 September 2015. Y-axis is the height from site deployment to 2000 m ASL, X-axis is the time in UTC, signal count scale range between 0-10,000.

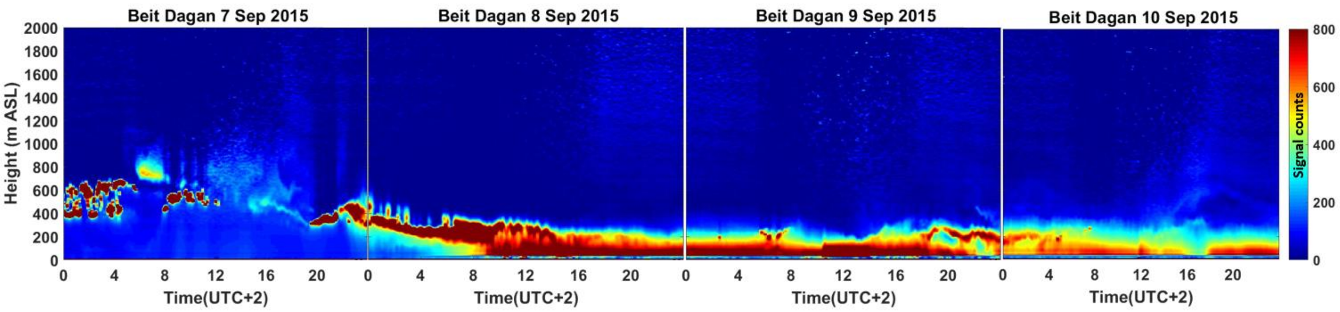

Figure 9. Beit Dagan ceilometer signal counts plots for 7-9 September 2015. Y-axis is the height from site deployment to 2000 m ASL, X-axis is in LST (UTC+2), signal count scale range between 0-800.

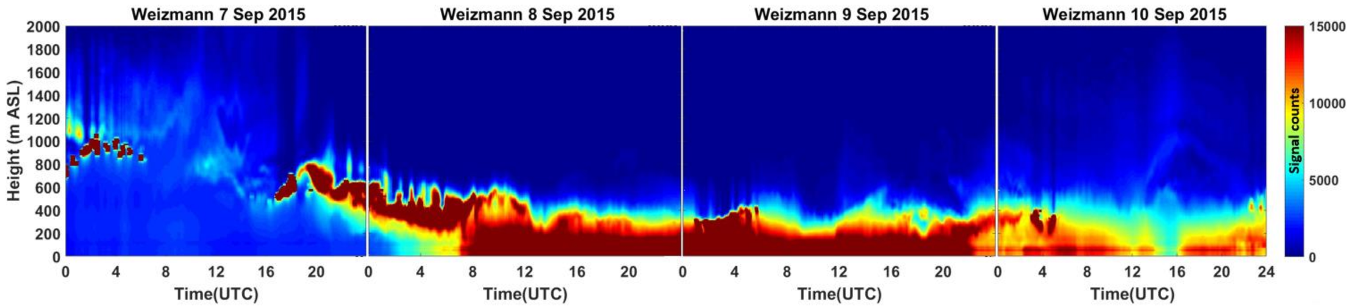

Figure 10. Weizmann ceilometer signal counts plots for 7-9 September 2015. Y-axis is the height from site deployment to 2000 m ASL, X-axis is in UTC, signal count scale range between 0-15,000.

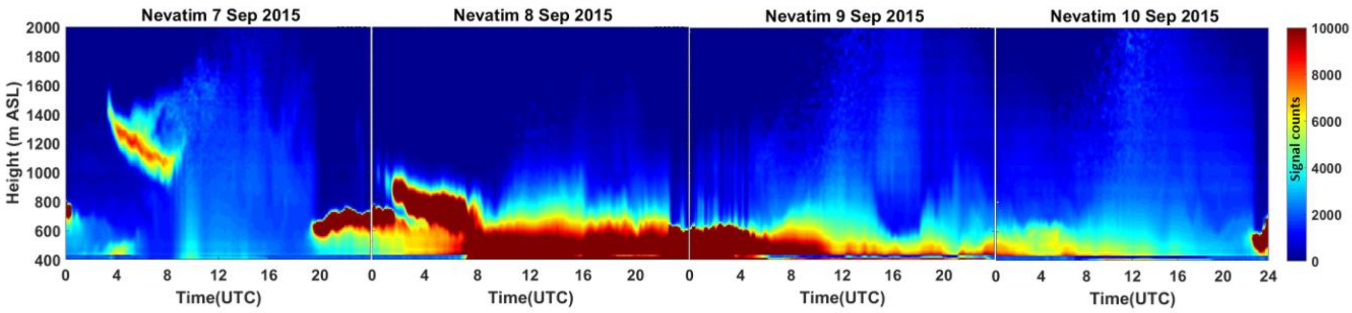

Figure 11. Nevatim ceilometer signal counts plots for 7-9 September 2015. Y-axis is the height from site deployment to 2000 m ASL, X-axis is the time in UTC, signal count scale range between 0-10,000.

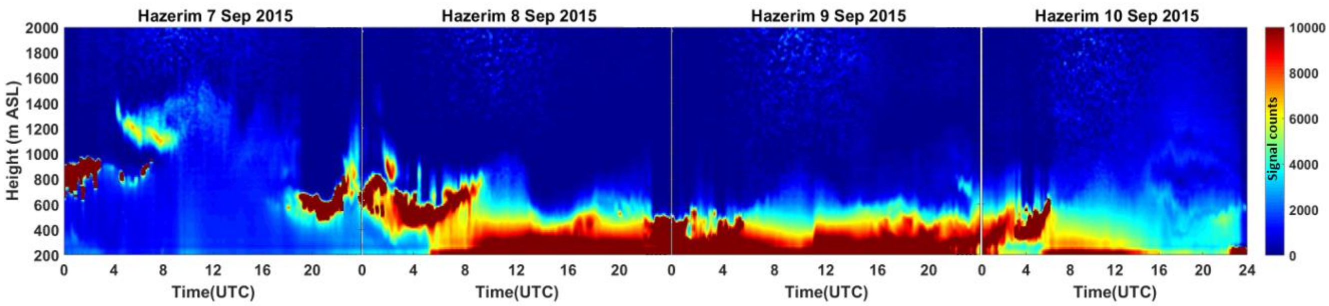

Figure 12. Hazerim ceilometer signal counts plots for 7-9 September 2015. Y-axis is the height from site deployment to 2000 m ASL, X-axis is the time in UTC, signal count scale range between 0-10,000.

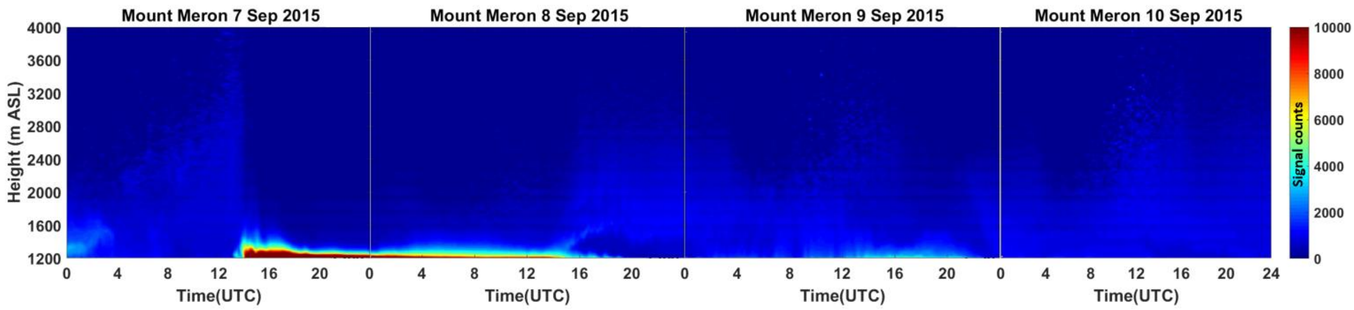

Figure 13. Mount Meron ceilometer signal counts plots for 7-9 September 2015. Y-axis is the height from site deployment to 2000 m ASL, X-axis is the time in UTC, signal count scale range between 0-10,000.

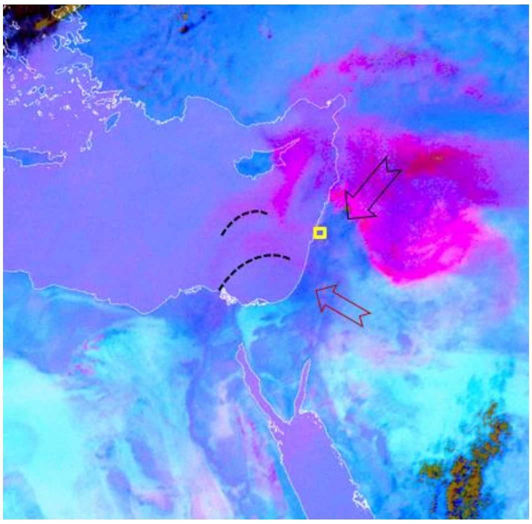

Figure 14. Picture from MSG-SEVIRI satellite of the dust RGB component (dust appears in pink colors) at 12 UTC 7 September 2015 with indications of Mount Meron ceilometer site (yellow square, Lon 33.0˚, Lat 35.4˚) and the dust plumes progression from east to west (red arrow and dashed lines) and from the northeast to southwest (black arrow).

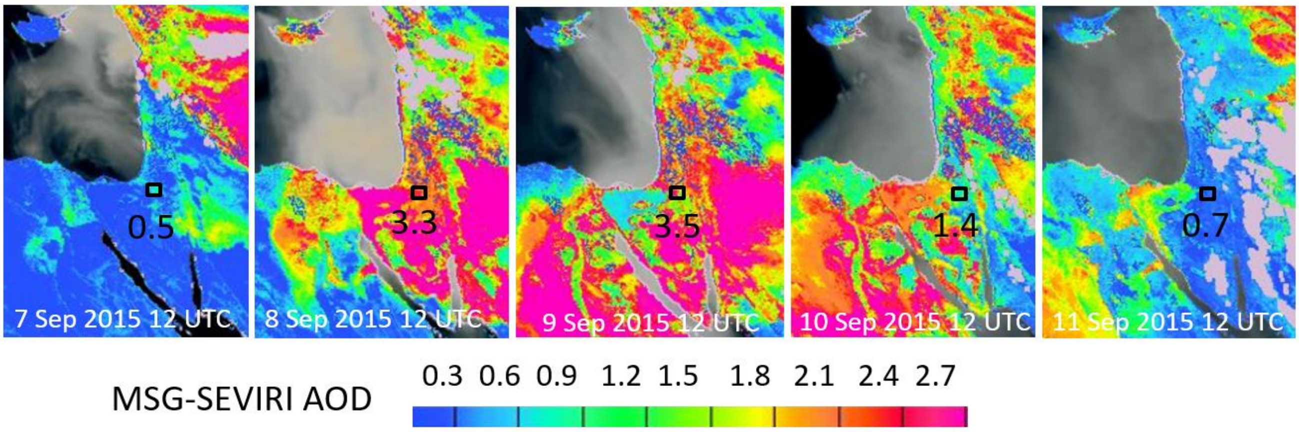

Figure 15. Aerosol Optical Depth (AOD) at 12 UTC 7-11 September 2015 analyzed by NAScube (Université de Lille) based on imagery from the MSG-SEVIRI satellite (by a combination of the SEVIRI IR8.7, IR10.8 and IR12.0 channels). The map includes indication of the Sede Boker AERONET site (black square) and its AOD value at 12 UTC.

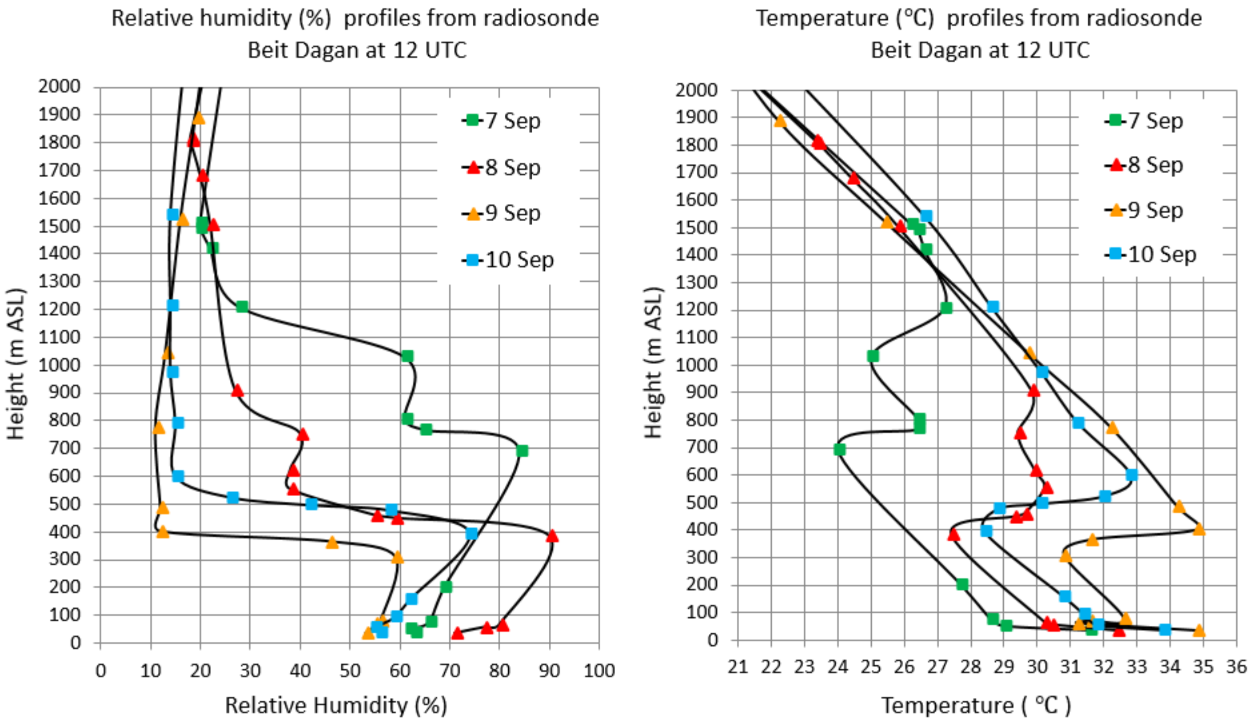

Figure 16. Radiosonde Beit Dagan profiles at 12 UTC between 7-10 September 2015 of relative humidity (left panel) and temperature (right panel).

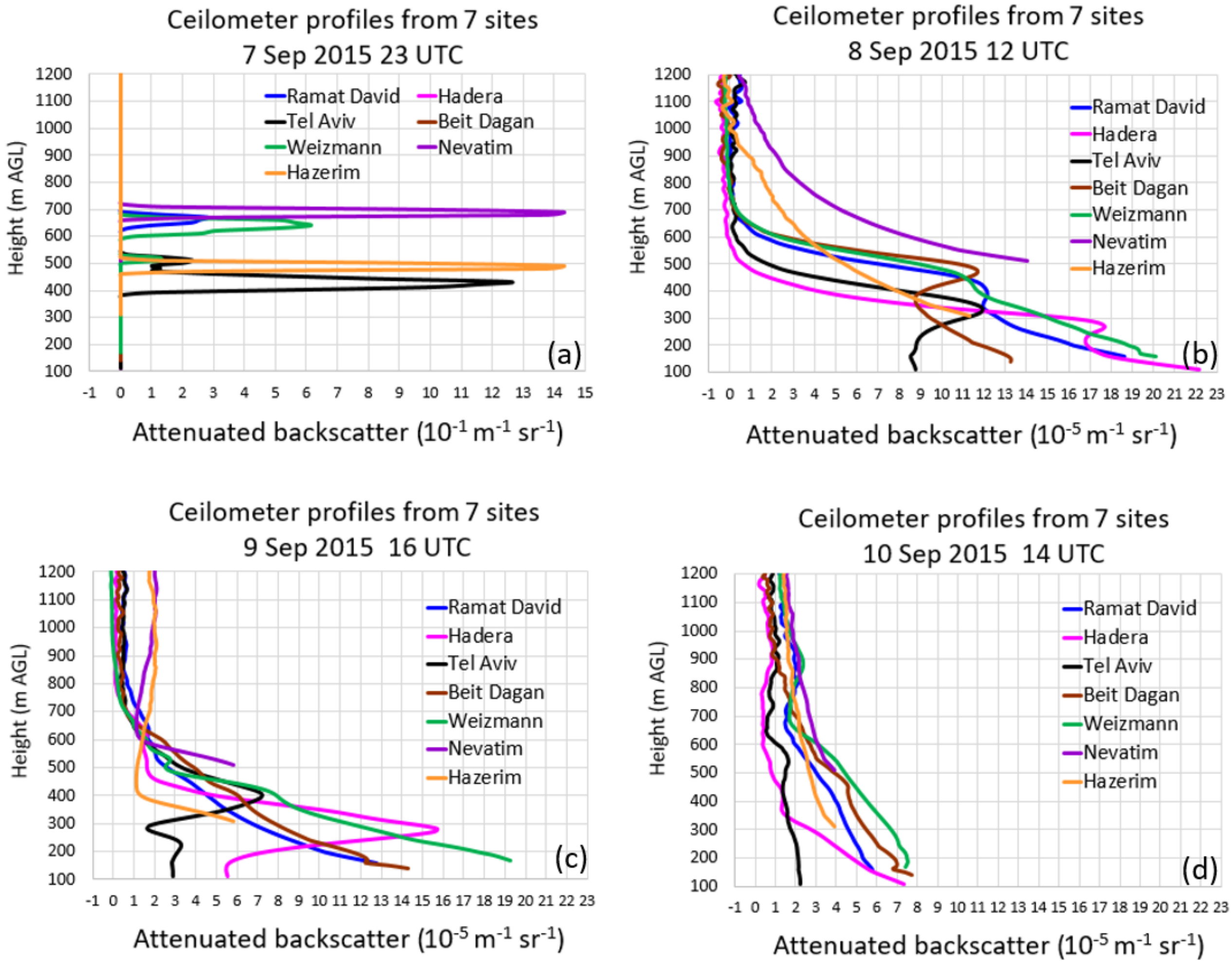

Figure 17. Ceilometer attenuated backscatter profiles from 7 sites (Ramat David, Hadera, Tel Aviv, Beit Dagan, Weizmann, Nevatim and Hazerim, Fig. 3) at 23 UTC 7 Sep 2015 (a), 8 September 2015 at 12 UTC (b), 9 September 2015 at 16 UTC (c) and 10 September 2015 at 14 UTC (d). Notice each profile begins relative to the height of its' measuring site (ASL) including a deletion of the first 100 m AGL due to inaccuracies in the first range gates of the CL31 ceilometers (for details see Sect. 2.1). Fig (a) shows cloud detection therefore it has a different scale (10^{-1} m^{-1} sr^{-1}) and a different x-axis range.

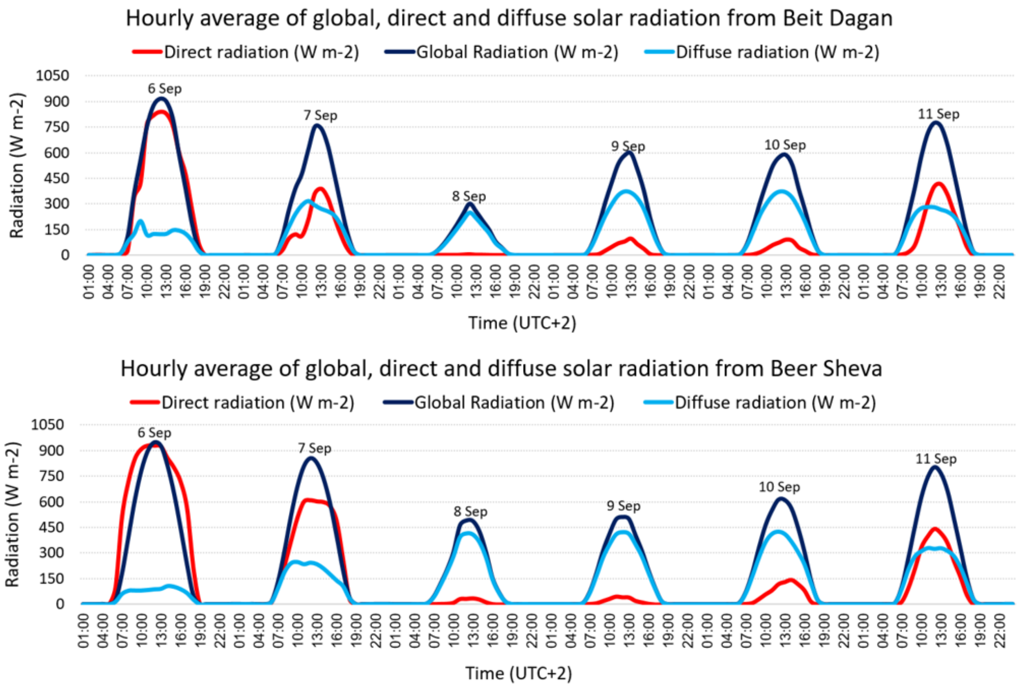

Figure 18. Hourly average of global, direct and diffuse solar radiation between 6-11 September 2015 from Beit Dagan and Beer Sheva.

The main phase (the peak) of the dust storm occurred on 8 September. Images from MODIS Aqua (Fig. 4b) and MODIS Terra (Fig. 4f) taken between 08:00-11:15 UTC show the dust storm prevalence over Israel. Ceilometers' plots detect the descending motion of the dust plume reached ground level at ~ 08 UTC (Fig. 6-12). Simultaneously, Sede Boker AERONET AOD measurements increased up to ~4 along with a negative Angström exponent (not shown).

An hour later, at ~ 09 UTC, extreme maximum PM hourly values were measured in the elevated sites of Jerusalem Safra (10,280 µg m^{-3} PM10) and Jerusalem Bar Ilan (3,063 µg m^{-3} PM2.5). Whereby, in the coast and the lower northern regions, maximum PM values were measured only 14 hours later at ~23 UTC and were much lower (up to 3,459 µg m^{-3} PM10 and 470 µg m^{-3} PM2.5, see Tables 5-6). Fig. 19 illustrates the spatio-temporal variation of the PM10 extreme values, beginning at ~ 12 UTC in the elevated Jerusalem sites and ending at midnight in the shoreline.

Ceilometer plots from Tel Aviv, Hadera (with plot range of 0-15,000, not shown here), Beit Dagan and Weizmann, reveal a two-layer shape, (beneath and above ~ 300 m ASL) starting from ~08 UTC. This two-layer shape later on combined into one dense layer. This pattern may explain the spatial variation and time delay between the extreme PM measurements in the elevated vs. lower sites.

Referring to satellite imagery on 8 September, MSG-SEVIRI at 12 UTC (Fig. 15) underestimated AOD to be 2.7 while Sede Boker AERONET measured a higher value of 3.3. Furthermore, MODIS images (Fig. 4a, 4b) show a dominant dust plume over Israel, while solar global radiation measurements (Fig.20a) show significant spatial variations in the reduction of the global radiation measured in the different regions. Minimum values down to 200 W m^{-2} were measured mainly in northern Israel. This may infer the complex behavior of the dust dispersion in contrary to satellite imagery of a prevailing dust storm over Israel. Additionally, in spite the extreme PM10 values of 9,031 µg m^{-3} measured in the elevated southern site (Negev Mizrahi 577 m ASL, Table 6), the maximum global radiation in southern Israel was still relatively high (~500 W m^{-2}).

Overall, 8 September shows the highest PM concentrations and the lowest solar radiation levels for this dust storm event. The solar radiation was composed mainly of diffuse radiation (Fig.18) emphasizing the immense atmospheric dust loads preventing direct insolation. Surprisingly, the low solar radiation was still able to warm the ground and generate a late and weak sea breeze front (not shown). We assume the insufficient ground heating generated thermals that were too weak to create and inflate a MLH. Therefore, we assume the low MLH (300 m ASL) revealed by the Beit Dagan profiles from 8 September (Fig.16) which may indicate the dust plume base height.

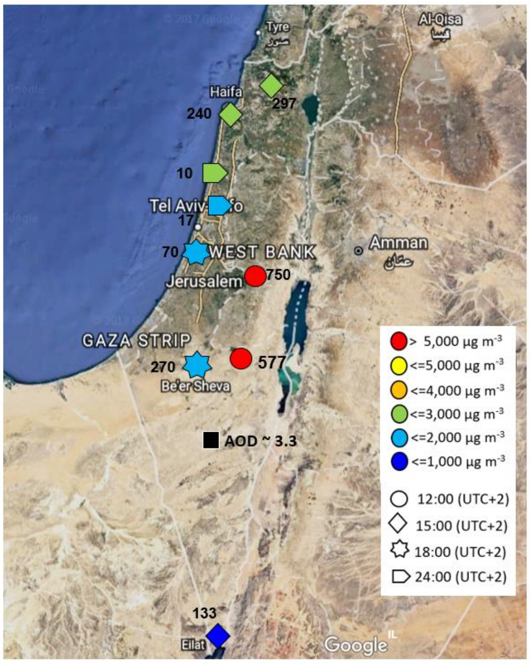

Figure 19. A map of PM10 maximum hourly concentration from 9 sites measured at 10 UTC on 8 September 2015. The map includes indications of the time of measurement (symbol shape), concentration range (symbol color), height of measurement site (numbers in black) and AERONET AOD from Sede Boker site.

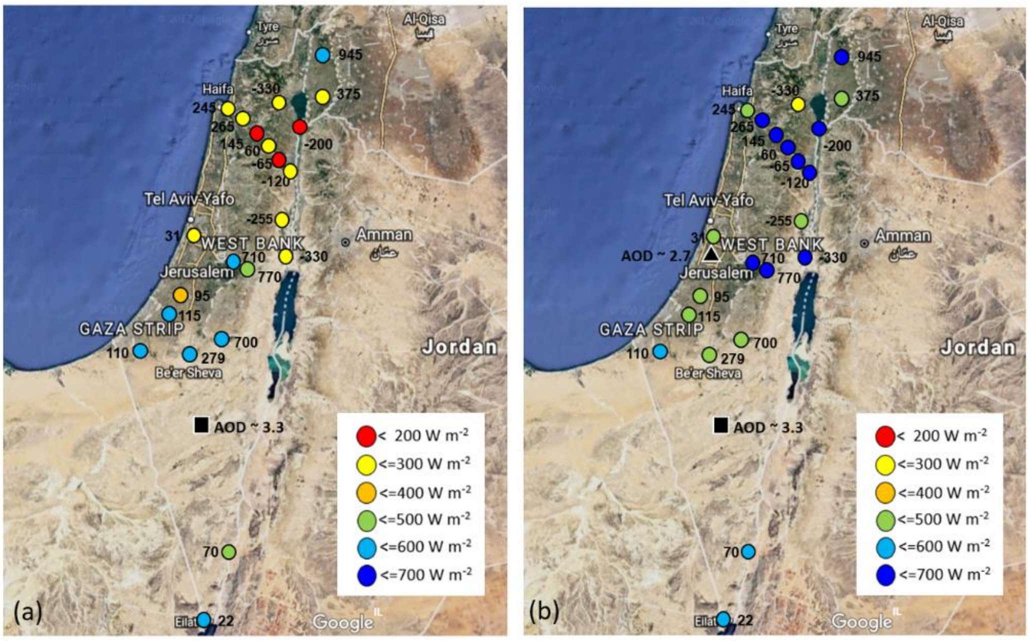

Figure 20. A map of maximum global solar radiation from 22 sites measured at 10 UTC (midday) on 8 September 2015 (a) and 9 September 2015 (b). The map includes indications of radiation range (see legend), height of measurement site (numbers in black) and AERONET AOD from Sede Boker site (black square) and Weizmann site (black triangle). On 8 September Weizmann AERONET did not operate.

.

On 9 September, MODIS images (Fig.4c and 4g) taken between 07:05-12:00 UTC show the dust plume progression southward to Egypt (Fig. 4), indicated by Sede Boker AERONET AOD >3 and a negative Angström exponent (Fig. 5). Again, an underestimation of AOD MSG-SEVIRI at 12 UTC shows lower AOD~ 2.7 compared to Sede Boker AERONET AOD ~ 3.5 (Fig.15). In contrary to the high AOD measurements, and the descend of the MLH down to ~ 350 m ASL (Fig.16), PM values did not crease but rather decrease below 900 µg m^{-3} PM2.5 (Table 5) and 4050 µg m^{-3} PM10 (Table 6). The drop in PM concentration gave rise to an increase of solar radiation of up to 400 W m^{-2} (Fig. 20 b). An increase in solar radiation enables significant ground heating to temperature values measured prior to the initiation of the dust storm (not shown). Thus, allowing generation of thermals and the creation of the sea breeze cycle which eventually produced an arc shape dust ascent visible in mainly in Tel Aviv and

Hadera coastal ceilometers beginning at ~ 12 UTC (Fig.7-8). Interestingly on 9 September, compared to the peak of the dust storm on the day before, we do not see a significant difference in solar radiation in southern Israel, which continued to be relatively high ~500 W m^{-2} (Fig. 20b).

On 10 September, MODIS pictures from 7:50 -11:05 UTC (Fig. 4d and 4h) show the dust plume over Israel transported southeast from Syria-Iraq to Sinai-Egypt. The CALIPSO single overpass Israel at 11:00-11:10 UTC revealed a dust layer between 2-4 km ASL (Fig.21). This corresponds with the EARLINET lidar measurements in Limassol, Cyprus (Mamouri et al., 2016) detecting a dust plume between 1-3 km ASL. We assume the CALIOP lidar did not produce data beneath 2 km ASL due to total attenuation. Fortunately, the ceilometers complement the dust profile (beneath 1~ 1 km ASL) showing a reduction both in signal counts (Fig. 6-12) and in attenuated backscatter profiles (Fig.17d) pointing out a reduction in atmospheric dust loads. AOD from MSG-SEVIRI and Sede Boker AEONET show a decrease down to (~1.5) and a low Angström exponent of ~0.5 indicating prevalence of mineral dust.

Furthermore, a profound reduction in PM values, down to a third of the values from the day before (Table 6), was measured mainly in southern Israel. Therefore, an increase in direct radiation (therefore an increase in global radiation as well) was measured in southern site as well (Fig.18). The reduction of dust loads may also be denoted by the orange background color of the photograph on the 8 September (Fig.1b) compared to the grey background visible on 10 September (Fig.1c). As the dust storm dissipated cloud formation was visible from at ~4 UTC by ceilometers plots from Ramat David (Fig.6), Tel Aviv (Fig.8), Weizmann (Fig.10) and Hazerim (Fig.11) (indicated by brown spots and evaluated by ceilometer profiles -not shown), otherwise not evident by MODIS imagery (Fig 4d, 4h).

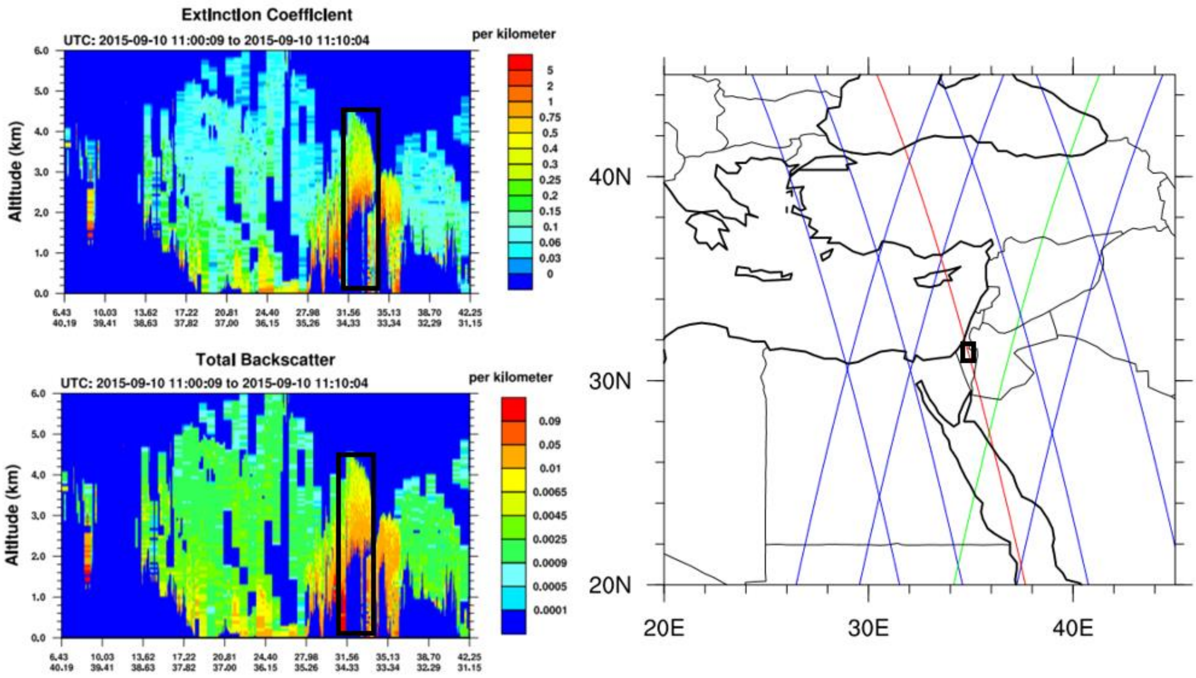

Figure 21. A map of CALIPSO satellite overpasses (right panel). The only overpass above Israel was on 10 September 2015 at 11:00-11:10 UTC (indicated by a red line). On the left panel are the CALIOP lidar products of total backscatter and extinction coefficient. Indications of the overpass over Israel is given by a black rectangle.

As the dust storm continues to dissipate over Israel, we analyzed measurements from all instruments regarding values measured prior to the dust storm penetration. While AERONET AOD (Fig.5) and satellite imagery from MODIS and SEVIRI (not shown) detect clearance of the dust storm on 17 September. PM and ceilometer profiles indicate the dust storm ended 4 days earlier at 13 September (not shown). This postulates a scheme of two dust levels or multiple sources of the dust plumes, which may support similar conclusions from previous studies (Stavros et al, 2016; Mamouri et al, 2016, Gasch et al, 2017).

4. Conclusions

A very severe dust storm struck the EM on September 2015. Previous investigations including in situ and remote sensing measurements and models discussed the initiation of the dust storm in the Syrian-Iraqi border, the limitations of the models to forecast this unique event, and several aspects of its transport over the EM. The analysis concentrated mainly on the upper level of the atmosphere and analyzed specific time segments of the dust storm period. The benefit here is the provision of vertical profiles of the dust in the lower part of the troposphere and the continuous measurements at 8 sites in Israel.

This study confirmed that the dust storm entered Israel on 7 September and showed the gradual downfall of the dust plume from ~1000m ASL on 7 September down to ~400 m ASL on 8 September. The detailed ceilometer profiles and auxiliary instruments enabled to separate the dust storm into two dust layers (beneath and above 1 km) and show a complex dispersion which would have been challenging for meso-scale model simulations. As the dust plume descended towards ground level on 8 September, PM concentration increased in the elevated stations (up to 10,280 µg m^{-3} PM10) and radiation decreased down to ~200 W m^{-2} mainly in the northern region. On 9 September as the dust plume diluted, in spite of the high AOD >3, the global radiation (mainly comprised of diffuse radiation) increased, thus enabling the ground heating and the creation of a late sea breeze circulation (~12 UTC) visible as dust arcs near the coast sites (Tel Aviv, Hadera and Beit Dagan). On 10 September, the dust plume motion continued southwest to Egypt, with indication of a dust layer between 2-4 km measured by CALIPSO overpass. The progress of the dust storm from the Syria-Iraqi border (origin) southwest to Egypt over Israel, continued in two levels. The lower level (up to 1 km ASL) dissipated at 13 September while the level aloft (above 1 km ASL) was observed until 17 September.

5. Data availability

PM10 measurements- Israeli Environmental ministry air quality monthly reports: http://www.svivaaqm.net.

Israeli Environmental ministry air quality monthly reports (in Hebrew): http://www.sviva.gov.il/subjectsEnv/SvivaAir/AirQualityData/NationalAirMonitoing/Pages/AirMoritoringReports.aspx.

Weather reports- Israeli Meteorological Service September monthly report (in Hebrew): http://www.ims.gov.il/IMS/CLIMATE/ClimateSummary/2015/hazesept+2015.htm

Radiosonde profiles –University of Wyoming: http://weather.uwyo.edu/upperair/sounding.html.

AERONET data- https://aeronet.gsfc.nasa.gov.

Meteosat Second Generation Spacecraft pictures:
http://nascube.univ-lille1.fr/cgi-bin/NAS3_v2.cgi.
https://www.eumetsat.int/website/home/Images/RealTimeImages/index.html

Ceilometer profiles- the data is owned by governmental offices. The data is not online and provided by request.

Author contribution

Leenes Uzan carried out the research and prepared the manuscript under the careful guidance of Smadar Egert and Pinhas Alpert. The authors declare that they have no conflict of interest.

Acknowledgements

We wish to thank the Israeli Meteorological Service (IMS), the Israeli Air Force (IDF), Association of towns for environmental protection (Sharon-Carmel) and Rafat Qubaj from the department of Earth and Planetary Science in the Weizmann institute of Science, for their ceilometers' data. Special thanks to Nir Stav (IMS) and Dr. Yoav Levy (IMS) for their fruitful advice, Anat Baharad (IMS) for computer assistance and Pavel Kunin from the Tel Aviv university, for the CALIPSO images. We thank the principal investigators Prof. Arnon Karnieli and Prof. Yinon Rudich for their effort in establishing and maintaining Sede Boker and Weizmann AERONET sites. We wish to thank the institutes that provide open site data reduction: Université de Lille NAScube site, Wyoming University Radiosonde site and Israeli ministry of Environmental protection for the PM data. Partial funding of this research was made by the Virtual Institute DESERVE (Dead Sea Research Venue).

References

Alpert P., Osetinsky I., Ziv B. and Shafir H.: A new seasons definition based on the classified daily synoptic systems: An example for the Eastern Mediterranean, Int. J. Climatol. 24,1013-1021, 2004.

Alpert, P., Ziv, B.: The Sharav cyclone-observations and some theoretical considerations, Int. J. Geoph. Res., 94, 18495-18514, 1998.

Ansmann, A., Petzold, A., Kandler, K., Tegen, I.N.A., Wendisch, M., Mueller, D., Weinzierl, B., Mueller, T. and Heintzenberg, J.: Saharan Mineral Dust Experiments SAMUM–1 and SAMUM–2: what have we learned? Tellus B, 63(4), 403-429, 2011.

Bennouna, Y.S., De Leeuw, G., Piazzola, J. and Kusmierczyk-Michulec, J.: Aerosol remote sensing over the ocean using MSG-SEVIRI visible images. Journal of Geophysical Research: Atmospheres, 114(D23), 2009.

Continuous measurement of PM10 suspended particulate matter (SPM) in ambient air, Center for Environmental Research Information Office of Research and Development U.S. Environmental Protection Agency Cincinnati, OH 45268 June 1999.

Dayan U., Lifshitz-Golden B., and Pick K.: Spatial and structural variation of the atmospheric boundary layer during summer in Israel-profiler and rawinsonde measurements, J. Appl. Meteo. 41, 447-457, 2002.

Derimian, Y., Karnieli, A., Kaufman, Y.J., Andreae, M.O., Andreae, T.W., Dubovik, O., Maenhaut, W., Koren, I. and Holben, B.N.: Dust and pollution aerosols over the Negev desert, Israel: Properties, transport, and radiative effect, J. Geophys. Res., 111, D05205 (1-14), 2006.

Donner, L.J., Wyman, B.L., Hemler, R.S., Horowitz, L.W., Ming, Y., Zhao, M., Golaz, J.C., Ginoux, P., Lin, S.J., Schwarzkopf, M.D. and Austin, J.: The dynamical core, physical parameterizations, and basic simulation characteristics of the atmospheric component AM3 of the GFDL global coupled model CM3, Journal of Climate, 24(13), 3484-3519, 2011.

Dubovik, O., A. Smirnov, B. N. Holben, M. D. King, Y. J. Kaufman, T. F. Eck, and Slutsker I.: Accuracy assessments of aerosol optical properties retrieved from Aerosol Robotic Network (AERONET) Sun and sky radiance measurements, J. Geophys. Res., 105(D8), 9791–9806, 2000.

Gasch, P., Rieger, D., Walter, C., Khain, P., Levi, Y., Knippertz, P., and Vogel, B.: Revealing the meteorological drivers of the September 2015 severe dust event in the Eastern Mediterranean, Atmos. Chem. Phys., 17, 13573-13604, 2017.

Haeffelin M., Angelini F., et al: Evaluation of Mixing –Height Retrievals from Automatic Profiling Lidars and Ceilometers in View of Future Integrated Networks in Europe. Boundary-layer Meteorol., 143,49-75, 2012.

Holben, B.N., Eck, T.F., Slutsker, I., Tanre, D., Buis, J.P., Setzer, A., Vermote, E., Reagan, J.A., Kaufman, Y.J., Nakajima, T. and Lavenu, F.: AERONET—A federated instrument network and data archive for aerosol characterization. Remote sensing of environment, 66(1), 1-16, 1998.

Hsu, N.C., Jeong, M.J., Bettenhausen, C., Sayer, A.M., Hansell, R., Seftor, C.S., Huang, J. and Tsay, S.C.: Enhanced Deep Blue aerosol retrieval algorithm: The second generation. Journal of Geophysical Research: Atmospheres, 118(16), 9296-9315, 2013.

Jasim, F.H., Investigation of the 6-9 September 2015 Dust Storm over Middle East, AJER, 5 (11), 201-207, 2016.

Jolivet, D., Ramon, D., Bernard, E., Deschamps, P.Y., Riedi, J., Nicolas, J.M. and Hagolle, O.: Aerosol monitoring over land using MSG/SEVIRI. In Proceeding of the EUMETSAT Meteorological Satellite Conference, Darmstadt, Germany ,8-12, 2008.

Kaskaoutis, D.G., Kambezidis, H.D., Nastos, P.T. and Kosmopoulos, P.G.: Study on an intense dust storm over Greece. Atmospheric Environment, 42(29), 6884-6896, 2008.

Koschmieder H.: Theorie der horizontalen sichtweite, Beitrage zur Physik der Freien Atmosphare 12, 33–55,171–181, 1924.

Kotthaus, S., O'Connor, E., Münkel, C., Charlton-Perez, C., Gabey, A. M., and Grimmond, C. S. B.: Recommendations for processing atmospheric attenuated backscatter profiles from Vaisala CL31 Ceilometers. Atmos. Meas. Tech., 9, 3769-3791, 2016.

Levi Y., Shilo E., Setter I.: Climatology of a summer coastal boundary layer with 1290-MHz wind profiler radar and a WRF simulation. J. Appl. Meteo., 50(9), 1815-1826, 2011.

Mamouri, R.E., Ansmann, A., Nisantzi, A., Solomos, S., Kallos, G. and Hadjimitsis, D.G.: Extreme dust storm over the eastern Mediterranean in September 2015: satellite, lidar, and surface observations in the Cyprus region, Atmos. Chem. Phys., 16(21), 13711-13724, 2016.

Mei, L., Xue, Y., de Leeuw, G., Holzer-Popp, T., Guang, J., Li, Y., Yang, L., Xu, H., Xu, X., Li, C. and Wang, Y.: Retrieval of aerosol optical depth over land based on a time series technique using MSG/SEVIRI data. Atmospheric Chemistry and Physics, 12(19), 9167–9185, 2012.

Mona, L., Liu, Z., Müller, D., Omar, A., Papayannis, A., Pappalardo, G., Sugimoto, N. and Vaughan, M.: Lidar measurements for desert dust characterization: an overview. Advances in Meteorology, 2012.

Münkel C., Emeis S., Muller J. W., Schäfer K.: Aerosol concentration measurements with a lidar ceilometer: results of a one year measuring campaign, Remote sensing of Clouds and the Atmosphere VIII, 5235, 486-496, 2004.

Münkel, C., Schäfer, K. and Emeis, S.:Adding confidence levels and error bars to mixing layer heights detected by ceilometer, In Proc. SPIE, Vol. 8177, 817708-1, 2011.

Papayannis, A., Amiridis, V., Mona, L., Tsaknakis, G., Balis, D., Bösenberg, J., Chaikovski, A., De Tomasi, F., Grigorov, I., Mattis, I. and Mitev, V.: Systematic lidar observations of Saharan dust over Europe in the frame of EARLINET (2000–2002). Journal of Geophysical Research: Atmospheres, 113(D10), 2008.

Parolari, A.J., Li, D., Bou-Zeid, E., Katul, G.G. and Assouline, S.: Climate, not conflict, explains extreme Middle East dust storm, Environ. Res. Lett, 11, 114013, 2016.

Pu, B. and Ginoux, P.: The impact of the Pacific Decadal Oscillation on springtime dust activity in Syria, Atmos. Chem. Phys., 16(21), 13431-13448, 2016.

Rao, P.G., Hatwar, H.R., Al-Sulaiti, M.H. and Al-Mulla, A.H.: Summer shamals over the Arabian Gulf. Weather, 58(12), 471-478, 2003.

Remer, L.A., Tanre, D., Kaufman, Y.J., Levy, R. and Mattoo, S.: Algorithm for remote sensing of tropospheric aerosol from MODIS: Collection 005. National Aeronautics and Space Administration, 1490, 2006.

Rieger, D., Bangert, M., Bischoff-Gauss, I., Förstner, J., Lundgren, K., Reinert, D., Schröter, J., Vogel, H., Zängl, G., Ruhnke, R. and Vogel, B.: ICON-ART 1.0-a new online-coupled model system from the global to regional scale. Geosci. Model Dev., 8, 1659–1676, 2015

Roebeling, R. A., Feijt A. J., and Stammes P.: Cloud property retrievals for climate monitoring: Implications of differences between Spinning Enhanced Visible and Infrared Imager (SEVIRI) on METEOSAT-8 and Advanced Very High Resolution Radiometer (AVHRR) on NOAA-17, J. Geophys. Res., 111(D20), 2006.

Romano, F., Ricciardelli, E., Cimini, D., Di Paola, F. and Viggiano, M.: Dust Detection and Optical Depth Retrieval Using MSG-SEVIRI Data. Atmosphere, 4(1), 35-47,2013.

Solomos, S., Ansmann, A., Mamouri, R.-E., Binietoglou, I., Patlakas, P., Marinou, E., and Amiridis, V.: Remote sensing and modeling analysis of the extreme dust storm hitting Middle East and Eastern Mediterranean in September 2015, Atmos. Chem. Phys., 17, 4063-4079, 2017.

Stull R. B.: An introduction to boundary layer meteorology, Kluwer Academic publishers, Netherlands, 666p, 1988.

Uzan L., Alpert P.: The coastal boundary layer and air pollution- A high temporal resolution analysis in the East Mediterranean Coast, The open atmospheric science journal, 6 ,9-18, 2012.

Uzan, L., Egert, S. and Alpert, P.: Ceilometer evaluation of the eastern Mediterranean summer boundary layer height–first study of two Israeli sites. Atmos. Meas. Tech., 9(9), 4387-4398, 2016.

Vaisala ceilometer CL31 user's guide M210482EN-B, October, 2004.

Wang, Y. Q.: MeteoInfo: GIS software for meteorological data visualization and analysis. Met. Apps, 21, 360–368, 2014.

Wiegner M. and Gasteiger J.: Correction of water vapor absorption for aerosol remote sensing with ceilometers, Atmos. Meas. Tech., 8, 3971–3984, 2015.

Wiegner, M., Madonna, F., Binietoglou, I., Forkel, R., Gasteiger, J., Geiß, A., Pappalardo, G., Schäfer, K. and Thomas, W.: What is the benefit of ceilometers for aerosol remote sensing? An answer from EARLINET, Atmos. Meas. Tech., 7(7), 1979–1997, 2014.

Winker, D.M., Vaughan, M.A., Omar, A., Hu, Y., Powell, K.A., Liu, Z., Hunt, W.H. and Young, S.A.: Overview of the CALIPSO mission and CALIOP data processing algorithms. Journal of Atmospheric and Oceanic Technology, 26(11), 2310-2323, 2009.

Table 1. The publications on the September 2015 dust event

Publications	Title	Main Tool	Main outcome
Pu, B. and Ginoux, P (2016)	The impact of the Pacific Decadal Oscillation on springtime dust activity in Syria	MODIS Terra MODIS Aqua DOD AOD, GFDL-AM3 model	Model underestimation in the EM due to inaccurate soil moisture
Parolari et al. (2016)	Climate, not conflict, explains extreme Middle East dust storm	WRF model	Unusual low level westerly wind spread to the EM, to reversely transport the previously eastward particles back to the EM.
Mamouri et al. (2016)	Extreme dust storm over the eastern Mediterranean in September 2015: satellite, lidar, and surface observations in the Cyprus region	MODIS, EARLINET profiles and PM10	Dust plumes from Syria entered the EM in a double layer structure, pointing to multiple dust sources
Stavros et al. (2016)	Remote sensing and modeling analysis of the extreme dust storm hitting Middle East and Eastern Mediterranean in September 2015	RAMS model EARLINET lidar, MSG and CALIPSO.	Low model ability to simulate the event, due to inaccuracies in model physical processes.
Jasim, F.H. (2016)	Investigation of the 6-9 September 2015 Dust Storm over Middle East	Satellite MSG-SEVIRI, Meteoinfo model	Two dust storms simultaneously, from northern Syria and Sinai desert created by two low pressure systems
Gasch et al. (2017)	An analysis of the September 2015 severe dust event in the Eastern Mediterranean	ICON-ART model	An unusual early active Red Sea Trough with meso-scale convective systems generating cold-pool outflows producing the dust storm. Model lacked development of a super critical flow to produce excessive wind speeds

Table 2. Ceilometers locations

Location	Site	Long/Lat	Distance from shoreline (km)	Height (m AGL)
Mount Meron	Northern	33.0/35.4	31	1,150
Ramat David	Northern	32.7/35.2	24	50
Hadera	Onshore	32.5/34.9	3.5	10
Tel Aviv	Onshore	32.1/34.8	0.05	5
Beit Dagan	Inland	32.0/34.8	7.5	33
Weizmann	Inland	31.9/34.8	11.5	60
Nevatim	Southern	31.2/34.9	44	400
Hazerim	Southern	31.2/34.7	70	200

*Ceilometer Weizmann is a CL51

Table 3. Ceilometers configurations

Location	Type	Time resolution(sec)	Height resolution (m)	*Height range (km)
Mount Meron	CL31	16	10	7.7
Ramat David	CL31	16	10	7.7
Hadera	CL31	16	10	7.7
Tel Aviv	CL31	16	10	7.7
Beit Dagan	CL31	15	10	7.7
Weizmann	CL51	16	10	15.4
Nevatim	CL31	16	10	7.7
Hazerim	CL31	16	10	7.7

* Height range dependents on sky conditions and is limited as AOD increases.
* In all ceilometers but in Beit Dagan site, data acquisition was limited to 4.5 km based on the BLview firmware

Table 4. Ceilometer technical information

Location	Type	Engine board	Receiver	Transmitter	Firmware
Beit Dagan	CL31	CLE311	CLR311	CLT311	1.72
Weizmann	CL51	CLE321	CLRE321	CLT521	1.03

Table 5. Hourly maximum concentration of PM2.5, collected from 21 monitoring sites, between 7-10 September 2015. The values are ranked from low (dark green) to high (dark red) values.

No.	Site	Height (m ASL)	Region	PM2.5 ($\mu g\ m^{-3}$) 7-Sep-15	8-Sep-15	9-Sep-15	10-Sep-15
1	Kefar Masarik	8	North	52	378	389	378
2	Ahuza	280	North	36	743	650	419
3	Newe Shaanan	240	North	43	400	466	525
4	Nesher	90	North	43	564	496	349
5	Kiryat Biyalic	25	North	53	424	703	447
6	Kiryat Binyamin	5	North	40	223	412	256
7	Kiryat Tivon	201	North	47	413	416	300
8	Afula	57	North	44	836	550	405
9	Raanana	54	Coast	38	173	291	229
10	Antolonsky	34	Coast	32	470	626	386
11	Ashdod	25	Coast	36	303	750	332
12	Ironi D	12	Coast	34	424	507	327
13	Tel aviv Central Station	29	Coast	41	716	803	451
14	Ashkelon	25	Coast	61	182	537	119
15	Jerusalem Efrata	749	Mountain	106	2285	434	403
16	Jerusalem Bar Ilan	770	Mountain	107	3063	641	518
17	Gedera	70	South	34	433	683	308
18	Nir Israel	30	South	25	363	638	228
19	Kiryat Gvaram	95	South	42	376	870	300
20	Sede Yoav	105	South	45	323	245	228
21	Negev Mizrahi	577	South	42	1748	526	317

Table 6. Hourly maximum concentration of PM10, collected from 31 monitoring sites, between 7-10 September 2015. The values are ranked from low (dark green) to high (dark red) values.

				PM10 (μg m^{-3})			
No.	Site	Height (m ASL)	Region	7-Sep-15	8-Sep-15	9-Sep-15	10-Sep-15
1	Galil Maaravi	297	North	114	3130	1987	1562
2	Karmelia	215	North	39	1120	1008	765
3	Newe Shaanan	240	North	104	3459	2471	1518
4	Haifa Port	0	North	78	1600	1965	1699
5	Nesher	90	North	117	3265	2746	1270
6	Kiryat Haim	0	North	82	1161	1625	1088
7	Afula	57	North	97	3239	2322	1961
8	Um El Kotof	0	Coast	99	2025	2028	1630
9	Orot Rabin	0	Coast	58	1152	1455	999
10	Barta	0	Coast	112	2540	2345	1612
11	Qysaria	19	Coast	54	1067	2116	1272
12	Rehuvot	70	Coast	88	2236	3045	1257
13	Givataim	0	Coast	112	1909	4014	1484
14	Yad Avner	77	Coast	61	1738	2902	1252
15	Ameil	20	Coast	96	2027	3472	1321
16	Shikun Lamed	17	Coast	51	1701	3244	1097
17	Station	29	Coast	87	1420	2176	998
18	Ashkelon	29	Coast	117	953	1692	551
19	Ariel	546	Mountain	128	2723	1481	1358
20	Jerusalem Efrata	770	Mountain	273	7820	1630	1437
21	Jerusalem Bar Ilan	749	Mountain	181	5588	1191	966
22	Jerusalem Safra	797	Mountain	491	10280	2389	1780
23	Gush Ezion	960	Mountain	310	6230	1679	1119
24	Erez	80	South	44	1000	1000	718
25	Beit Shemesh	350	South	115	2097	1943	1788
26	Carmy Yosef	260	South	85	1047	784	594
27	Modiin	267	South	185	2701	2245	1980
28	Bat Hadar	54	South	65	1342	2563	841
29	Nir Galim	0	South	94	1479	2292	1027
30	Negev Mizrahi	577	South	183	9031	2806	1730
31	Eilat	0	South	275	1867	1592	1684